Ultra-Low Thermal Conductivity in Dual Doped n-type Bi_2Te_3 Material for Enhanced Thermoelectric Properties

*Jamal-Deen Musah[1], Guo Chen[2], Andrei Novitski[3], Illia Serhiienko[3], Adesina Ayotunde E.[4], Vladimir Khovaylo[3,5,6], Chi-Man Lawrence Wu[2], Juan Antonio Zapien[4], Vellaisamy A.L. Roy[7]**

Affiliation:

[1]Department of Materials Science and Engineering and State Key Laboratory of Terahertz and Millimeter Waves, City University of Hong Kong, Kowloon Tong, Hong Kong S.A.R.

[2,4] Department of Materials Science and Engineering, City University of Hong Kong, Kowloon, Hong Kong S.A.R

[3]National University of Science and Technology "MISiS", Moscow 119049, Russia

[5]National Research South Ural State University, Chelyabinsk 454080, Russia

[6]Chelyabinsk State University, Chelyabinsk 454001, Russia

[7]James Watt School of Engineering University of Glasgow, United Kingdom

Abstract

Bismuth chalcogenides are promising materials for thermoelectric application due to their high power factor (product of the square of the Seebeck coefficient and electrical conductivity). However, their high thermal conductivity is a great issue of concern. Single doping has proven to be useful in improving thermoelectric performance in recent years. Here we show that dual isovalent doping shows the synergistic effect of thermal conductivity reduction and electron density control, which is crucial for the enhancement of power factor. The insertion of large atoms in the layered Bi_2Te_3 structure distorts the crystal lattice and hence contribute significantly to phonon scattering. The ultralow thermal conductivity (K_T = 0.35 $Wm^{-1}K^{-1}$ at 473K) compensates for the low power factor and thus leads to enhancement in the TE performance. Our density functional theory electronic structure calculation results reveal the formation of deep defects states in the valence band. The

creation of deep states influences the electronic transport properties of the system. The dual dopants (In and Sb) thus show a coupled effect of improvement in the density of state near the Fermi level and reduction in the conduction band minimum, thus resulting in the enhancement of electron density. Numerically, we demonstrate that the dual doping favours acoustic phonon scattering that creates an interference pattern for phonon transport and thus drastically reduces the lattice thermal conductivity for improving thermoelectric material efficiency.

KEYWORDS; Dual doping, Thermoelectric (TE), Bismuth Chalcogenides, Power Factor (PF), lattice distortion, isovalent substitution

---

*Corresponding author: roy.vellaisamy@glasgow.ac.uk

1. Introduction

Thermoelectric (TE) devices can be used as valuable solid-state converters of waste energy to useful electrical power with no moving parts. They are environmentally friendly and therefore serve as the best alternative for suitable power generation [1,2]. Their remarkable attraction includes the scalability, reliability and optimum utilization of technology for waste energy recovery. The dimensionless figure-of-merit characterizes a TE material performance, $ZT = \sigma S^2 T (k_{el} + k_{lat})^{-1}$, where σ, S, k_{el} , k_{lat} and T are the electrical conductivity, Seebeck coefficient, electronic thermal conductivity, lattice thermal conductivity and the absolute temperature, respectively. Traditional TE modules include Bi_2Te_3 – based devices for a room or near room temperature application[3] due to their considerably high power factor (PF). [2,4,5] An ideal TE material possess low thermal conductivity coupled with enhanced Seebeck coefficient and electrical conductivity[2]. However, simultaneous enhancement in S and σ is challenging due to their interdependency. This conflict, therefore, makes it challenging to improve the two transport properties simultaneously, thereby affecting the power factor (PF). Much attention is thus given to total thermal conductivity (k_T) reduction. It is assumed that thermoelectric materials should be heavily doped to yield high TE performance. [2]. In that case, the dopant(s) introduces extrinsic carriers into the host, which results in improvement of the electronic transport properties while decreasing the heat transport properties (via phonon scattering by the impurity atoms).

Bi_2Te_3 topological insulators remain the best room temperature (RT) TE materials due to their admiring thermoelectric performance [3]. Physical properties of materials are characteristic of the atomic arrangement and how it can accommodate defects in the crystal structure.[6,7] Creating lattice disorder (strain, dislocation), via doping is useful it reducing the K_T[8]. Metal chalcogenide structures are complex structures with voids[9] which allows for accommodating impurity atoms to enhance phonon scattering [2][10]. Thermal conductivity reduction via the creation of disorder within the unit cell shows dominance in structures containing voids. The layered structures of Bi_2Te_3 are responsible for its effective anisotropic mass (m*), which leads to an increase in the Seebeck coefficient with deterioration in electron mobility [11]. In this regard, the transfer of thermal energy via the materials is impeded, which thus leads to K_T reduction [12–17]. The narrow bandgap (0.15eV) and high band degeneracy of Bi_2Te_3 also increase PF [18]. This implies, provided, K_T is substantially reduced, the TE figure of merit (ZT) will be optimized. We recently, showed that cationic isovalent substitution in Bi_2Se_3 could produce a multifold enhancement in ZT via simultaneously improvement in S and σ and a corresponding decrease in total thermal conductivity.[19] In a similar work of Wu *et al.* [20] reveal the formation of deep defect state and a hyper deep defect state in GeTe material upon the introduction of In impurity. These states lead to the distortion of the density of state (DOS) near the Fermi level and therefore resulted in enhanced TE performance.

Herein, we report indium (In) and antimony (Sb) dual doping in bismuth telluride as a strategy for drastic lattice thermal conductivity reduction and hence decreases overall thermal conductivity. The dual doping in Bi_2Te_3 is synthesized through a one-step modified Wang *et al*. route. It is expected that the intercalation of Sb in Bi_2Te_3 crystal structure will fill the interstitial site while the isovalent substitution of In offers a substitute for the cation (Bi). This is aimed at creating an interference pattern for phonon transport and hence reduce the lattice thermal conductivity without substantially compromising the PF. Indium atom was chosen to substitute bismuth because both In and Bi have the same number of electrons associated with the valence states (i.e. $5s^25p^1$ for In and $6p^3$ for Bi). This type of doping (isovalent), therefore, lead to the formation of neutral impurities which have less effect

on conduction electrons scattering, unlike ionized impurities. Similarly, the ionic radii difference between the dopants (In^{3+}→0.91 Å, Sb^{3+}→0.9 Å)[21] and the host (Bi^{3+}→1.03 Å) create tolerance for substitution. Therefore, the substitution of In for Bi is favourable in sustaining the resulting materials crystal structure. Conventional doping (aliovalent) typically, promote excessive enhancement in the charge carrier density (either holes or electrons) which thus significantly deteriorate the Seebeck coefficient and hence the thermoelectric properties. However, isovalent substitution (such as In for Bi with equal charges, 3+) controls the carrier density and the only concern for improving the TE efficiency rely on the decrease of the thermal conductivity, which we have shown via the combined effect of the isovalent substitution (with In) and antimony (Sb) intercalation. Sb has demonstrated an excellent performance as a dopant in Bi chalcogenides thermoelectric materials in recent research due to the similar crystal structure of Sb_2Te_3 and Bi_2Te_3. But in most cases, Sb is used as a substitute for Bi in Bi_2Te_3 thermoelectric materials. However, considering the smaller atomic size of Sb (133 pm) compared to Bi (143 pm), we, therefore, used Sb to intercalate the $Bi_{2-x}In_xTe_3$ structure to enhance phonon scattering. The rattling of the Sb atoms in the van der Waals gaps of the $Bi_{2-x}In_xTe_3$ contribute to lattice thermal conductivity reduction cause by absorption of phonon vibration.

2. Experimental Section

2.1 Synthesis of Bi_2Te_3 and $Bi_{2-x}In_xSb_{2x/3}Te_3$ nanocostructures (x = 0, 0.05, 0.1, 0.2, 0.3)

Tellurium powder (Te powder, J&K Scientific Ltd, 99%), Bismuth (Bi) nitrate pentahydrate ($Bi(NO_3)_3.5H_2O$, J&K Scientific Ltd, 98%), Indium chloride (Aldrich, 99.99%), Antimony chloride (Aldrich, 99.99%) ethanolamine (ACS reagent, Aldrich ≥ 99.0%) and 2-methoxy ethanol anhydrous (Sigma Aldrich, 99.8%) were used without any further purification. First, 2-methoxy ethanol and ethanolamine were preheated at 373K for 30minutes. Then 1mmol of $Bi(NO_3)_3.5H_2O$ was measured and added to the above mixture, which was subjected to continuous stirring until all the crystals dissolve. Afterwards, 1.5 mmol of Te powder was then transferred into the above solution and kept under continuous stirring for 3 hours on a hot plate, which is kept at 473K. These same steps are

followed to prepare the dual doped composition. Finally, the hot plate was put off, and the precipitate was collected through centrifugation, followed by washing multiple times with water and ethanol. The obtained powder was then dried at 343K in an open oven for 6 hours. Details of the synthesis procedure are schematically shown in **Figure 1.**

2.2 Characterization of Bi_2Te_3 and $Bi_{2-x}In_xSb_{2x/3}Te_3$ nanostructures

The structural and morphological properties of the dual-doped Bi_2Te_3 composite were characterized by X-ray diffraction (XRD Bruker SRD –D2 Phaser), scanning electron microscopy (FEG-SEM, FEI Quanta 450), Raman spectroscopy (Renishaw 2000 Raman microscope equipped with a HeNe laser of 633nm excitation wavelength with laser power of 15 mW) and X-ray photoemission spectroscopy (PHI Model 5802). The results of the elemental composition are shown in **Figure S-1** ($Bi_2Te_{3-\delta}$) and **Figure S-2** (dual doping) in the Supporting Information (SI). The Bi_2Te_3 and the dual doped Bi_2Te_3 nanostructures were cold pressed and formed into a disc-shaped specimen (diameter, thickness and pressure of 13 mm, 0.7 mm and 20 MPa respectively). The cold-pressed pellets were then annealed at 523K, 573K and 623K for 12 hours in vacuum. This was followed by furnace cooling to RT. Variation of annealing temperature allowed us to control the amount of Te vacancies ($\boldsymbol{\delta}$). For ease in referencing our prepared samples , all the $Bi_2Te_{3-\delta}$ samples are abbreviated as follows: as-synthesized ($\delta = 0.01$), BT@523K ($\delta = 0.08$), BT@573K ($\delta = 0.15$) and BT@623K ($\delta = 0.25$) corresponding to the raw pellet, samples annealed at 523K, 573K and 623K respectively. It is worth mentioning that the maximum annealing temperature in this study is chosen to be 623K because, for the BT@623K sample, the amount of Te which sublimes reaches 8% which results in much distortion in the crystal lattice (due to deviation from stoichiometry). The evaporation temperature for tellurium is approximately 523 – 573K [22] and therefore, a post-synthesis temperature much higher than the stable temperature is detrimental for preserving stoichiometry for Te containing materials for TE device application. Accordingly, our thermogravimetric analysis (**Figure S-3**) shows the thermal stability of the Bi_2Te_3 in the temperatures less than 570K (linear region) with approximately 7% loss in the

sample weight when the annealing temperature was increased to 623K. Secondly, the electrical conductivity measurement shows the emergence of conduction type switch (from semiconducting to metallic) when the annealing temperature was increased to 623K which shows sufficient change in the crystal structure of the $Bi_2Te_{3-\delta}$ ($\delta = 0.25$) material due (excess Te loss) to its sensitivity to point defects. After the optimization study of the BT samples, the best performer was then taken and dual doped with In and Sb in other to further enhance the TE performance. Again, the $Bi_{2-x}In_xSb_{2x/3}Te_3$ (x = 0 , 0.05 ,0.1, 0.2, 0.3) samples are abbreviated as ; BT (x = 0) , BIST- 0.05 (x = 0.05), BIST- 0.1 (x = 0.1), BIST- 0.2(x = 0.2), BIST- 0.3 (x = 0.3). It should be noted that the BT@623K sample in the optimization study is the same as the BT sample in the dual doped section.

2.3 Thermoelectric properties measurement

The Seebeck coefficient (S), electrical conductivity (σ) and total thermal conductivity (k_T) of all the samples were measured from 300 K to 473 K. A rectangular bar-shaped (12.7 mm ×7 mm ×0.5 mm) samples were cut out from the 13 mm circular disc samples for the S and σ measurement (using ZEM instrument). Thermal diffusivity (λ) was carried out on a 12.7mm × 0.5 mm circular disc for all the samples using a laser flash diffusivity system (NETZSCH, LFA457). Similarly, the specific heat (Cp) and the density (ρ) were carried out using scanning calorimetry (NETZSCH, DSC 404F) and Archimedes principles, respectively. The error in the electrical conductivity and Seebeck coefficient measurements was within 8%, and that of the thermal conductivity measurements was within 9%. We, therefore, calculated the total thermal conductivity from the relation $k_T = \rho \times \lambda \times C_p$. The RT Hall coefficient, R_H, was measured using a commercial Hall-effect system (ECOPIA HMS-5300) in the van der Pauw configuration, under a magnetic field of 0.5T and a current of 20 mA. The Hall electron concentration, n_H, and the electron mobility, μ_H were calculated according to $n_H = \frac{1}{eR_H}$ and $\mu_H = \sigma R_H$ respectively.

2.4 Computational Detail

The density functional theory (DFT) was used to perform our calculation with the program package DMol[3] using the Perdew−Burke−Ernzerhof (PBE) of generalized-gradient approximation (GGA)

function. [23]. The $Bi_{2-x}In_xSb_{2x/3}Te_3$ structures were modelled by the 2 × 2 × 1 supercell. The DN basic set with polarization functions (DNP) in the electronic tab was taken to describe the whole system. The DFT Semi-core Pseudopots (DSPP) core treatment was used to replace core electrons by a single effective potential.[24] The k-point of the Brillion zone was set as 3 × 3 × 1 for the geometry optimization, and 6 × 6 × 3 for high-quality electronic structure calculation.

3. Results and Discussion

3.1 Structural Properties of the $Bi_2Te_{3-\delta}$ Bulk Materials

Figure S-4a depicts the XRD patterns of all $Bi_2Te_{3-\delta}$ samples, where an increase in annealing temperature shifts the XRD patterns to lower 2θ (**Figure S-4b**). All characteristic peaks of the bulks Bi_2Te_3 coincide well with the hexagonal phase (PDF # 85-0439) [25], showing the formation of a single-phase compound. It is also evident from the lattice parameters calculation [26] that, the presence of the Te vacancies result in a decrease in the lattice constants and volume. The measured Raman spectra (normalized) of all the synthesized $Bi_2Te_{3-\delta}$ ($\boldsymbol{\delta}$ = 0.01, 0.08, 0.15 and 0.25) bulk samples is shown in **Table S-1**. The three peaks at 98.8, 117.2 and 137.4 cm^{-1} are indexed to E_g^2, A_{1u} and $A^2{}_{1g}$ vibrational modes, respectively [27–29]**.** Increase in annealing temperature causes a shift in the Raman spectral. The observed Raman shift could be attributed to several reasons, (a) increase in the Te sublimation, resulting in the alteration of the chemical structure of the sample. Raman spectra shift to either higher or lower energy is usually observed when the chemical composition of the material is altered due to external influence [30]. Again, the V_{Te} modifies the lattice vibration and hence promote phonon electron interaction within the $Bi_2Te_{3-\delta}$ structure thus causing Raman shift (b) Enhancement in the crystallinity of Bi_2Te_3 materials with an increase in annealing temperature has been shown elsewhere to bring about a shift in Raman peaks [31]. **Figure S-5** displays the FEG-SEM images for all the $Bi_2Te_{3-\delta}$ (δ= 0.01, 0.08, 0.15, 0.25) pellet samples. The microscopic investigation of the fracture surface reveals an increase in compactness with increasing annealing temperature.

3.2 Thermoelectric Properties of the $Bi_2Te_{3-\delta}$ Bulk Materials

Numerical values for electron concentration n_H and electron mobility μ_H derived from Hall effect measurements at RT are displayed in **Table S-2**. It is seen that, as the annealing temperature increases, electron concentration(n_H), as well as the Hall mobility (μ_H), becomes more substantial. The simultaneous improvement in n_H and μ_H contributed to enhancement in both the Seebeck coefficient and the electrical conductivity with annealing temperature. It is established that the n_H in Bi_2Te_3 based materials is sensitive to point defects [32,33]. Usually, the annealing-induced point defects present in Bi_2Te_3 alloys are Te and Bi vacancies. In a typical case of *n*-type Bi_2Te_3 compounds, tellurium vacancies (V_{Te}) are easily formed due to the ease in the sublimation of Te (because of the low energy of evaporation of Te compared with Bi) thereby contributing a pair of electrons per V_{Te} (**Eqn 1**)

$$Bi_2Te_3 \equiv 2Bi_{Bi}^{\times} + (3-x)Te_{Te}^{\times} + xTe(g)\uparrow + xV_{Te}^{2+} + 2xe^{-} \quad (1)$$

Therefore, the improvement in the n_H is evident in the enhancement in the electrical properties.

Figure 2a depicts the temperature dependence of the measured electrical conductivity for all $Bi_2Te_{3-\delta}$ bulk samples. In the as-synthesized, BT@523K and BT@573K samples, the electrical conductivity increases with increasing temperature. This is because of several reasons: (1) as the annealing temperature increase, the crystallinity of the samples is enhanced. It should be mentioned that a high degree of crystallinity allows for high mobility with an improved density of state effective mass [34]. (2) as the temperature is further increased, excessive sublimation of Te occurs, thereby creating more Te vacancies.

These vacancies contribute to the electron concentration of the material, which leads to enhancement in the electrical conductivity. For the BT@623K sample, σ decreases from room RT to 500K, which is typical of a semi-metallic behaviour [35]. This shows a change in the conduction mechanism from semi-conducting (for as-synthesized, BT@523K and BT@573K samples) to semi-metallic (BT@623K samples) with annealing temperature due to the improvement in n_H. The RT

improvement in the S with the annealing temperature is as a result of the simultaneous increase in μ_H (See **Table S-2**) and the n_H caused by the sublimation of Te. **Figure 2b** shows the temperature dependence of the Seebeck coefficient in the studied $Bi_2Te_{3-\delta}$ materials. It was noticed that the measured RT Seebeck coefficient, S of all the samples increases with annealing temperature but decreases with measured temperature. The maximum value of the Seebeck coefficient, -174.6 μVK^{-1}, is found for the sample annealed at 623K.

Figure 2c is the data for the calculated power factor (PF) with temperature. The RT power factor for the as-synthesized sample is 114 $\mu Wm^{-1}K^{-2}$ which increased to 241 $\mu Wm^{-1}K^{-2}$ for the sample annealed at 523K. Upon further increase in annealing temperature (573K and 623K), the power factor was significantly enhanced up to 567 $\mu Wm^{-1}K^{-2}$ and 983 $\mu Wm^{-1}K^{-2}$ respectively. It can be seen that, as the annealing temperature increases, the RT power factor thus increases. The maximum PF of 983 $\mu Wm^{-1}K^{-2}$ is found for the sample annealed at 623K. This value represents 763%, 308% and 74% enhancement as compared with the samples without annealing and those annealed at 523K and 573K respectively.

Similarly, the improvement found in this work is about 294% (4 times) and 245% (3 times) larger than that reported by Zhao *et al.* [36] and Liu *et al.* [37] respectively. The enhanced performance exhibited by our sample is due to the improved purity and the controlled V_{Te} of the synthesized samples compared to that of Liu *et al*. and Zhao *et.al.* The temperature dependence of the K_T is shown in **Figure 2d**. The selected annealing temperatures introduce V_{Te} in the Bi_2Te_3 lattice, which increases lattice scattering. Thus, the total thermal conductivity decreases especially for the highest temperature of annealing (623K) due to the largest Te sublimation. The lowest total thermal conductivity is found for BT@623K (0.75 Wm^{-1} K^{-1} at 393K) temperature. From this study, 623K emerges as the best condition for the post-synthesis treatment of the Bi_2Te_3 samples, which thus demonstrate low thermal conductivity with high power factor and therefore shows the maximum ZT of 0.43 at 393K (**Figure 2e**).To further improve the performance of the BT@623K, we adopted dual doping of In and Sb as

discussed below. The same procedure described in **Figure 1,** was used to synthesis the dual doped samples.

3.3 Structural Properties of the $Bi_{2-x}In_xSb_{2x/3}Te_3$ Bulk Materials

X-ray diffraction technique is used to verify the crystal structure of the $Bi_{2-x}In_xSb_{2x/3}Te_3$ nanostructures. The normalized XRD patterns of all the synthesized nanostructures are shown in **Figure 3a**. From **Figure 3a**, it is obvious that, despite the dual doping of In and Sb in BT, a single-phase BIST is formed with all diffraction peaks well indexed to the hexagonal Bi_2Te_3 phase (PDF # 85-0439). However, there exist a noticeable peak shift to a lower 2θ, from 27.735 (x = 0) to 27.715 (x = 0.05). Upon increase in the doping content, 2θ further decreased until x = 0.1 (27.654). It is therefore observed that as more of In dopant substitutes the Bi host and the intercalate (Sb) content increases, the lattice expansion reaches its maximum (at x = 0.1). The shift of the peaks (**Figure S-6a**) to the lower 2θ for the less doped (x = 0.05 and x = 0.1) samples is due to the presence of lattice expansion of the BIST structure [38]. The high doping of In and Sb in Bi_2Te_3 materials (x = 0.2 and x = 0.3) degrades the crystal quality, which eventually affected the mobility and electrical properties significantly. However, the crystal structure was unchanged but shifted the XRD peaks to a lower 2θ as a response to the high doping. The dual doping of In and Sb offered no significant alteration to the chemical structure. If not, the Raman peak position would be altered, and a new peak would be evolved in the dual doped samples. Similarly, the XPS data shows no significant difference in the binding energies between the pristine and the doped samples thus confirming that the excess doping of the In and Sb (x = 0.2 and x = 0.3) did not promote composite formation (within the detection of the XRD instrument) but degraded the crystallinity of the samples. More importantly, indium substitution in bismuth ($Bi_{2-x}In_xTe_3$ for x = 0.375) reported by Liu *et al.* [39] still retained the hexagonal structure of the Bi_2Te_3 system. Similarly, Lutetium and Selenium dual substitution in $Lu_xBi_{2-x}Te_{2.7}Se_{0.3}$ reported by Cao *et al.*[40] for $0 \leq x \leq 0.3$ showed no evolution of extra

XRD peaks. This is because the layered structures and flexibility of Bi_2Te_3 materials enable the accommodation of foreign materials.

More so, the peak intensity (**Figure S-6b**) increases slowly from the undoped sample to x = 0.1 and then declines sharply until x = 0.3. The peak intensity is associated with the crystal quality of the prepared samples. The crystallinity increases from x = 0 to x = 0.1 which then decreases upon further doping. This is shown in **Figure S-6c**, where we have estimated the degree of crystallinity using **Eqn S-1**. It is thus shown that the dual dopants with different ionic radii compared to that of the host does not only create lattice distortion but also degrade the crystallinity of the pristine structure. The calculated lattice parameters (a and c) and the volume (v) shown in **Figure 3b** were obtained using the procedure in Ref.[27]. Variations in the lattice parameters are attributed to the incorporation of the dopants in the intrinsically layered structure of the Bi_2Te_3. The lattice parameters increase with the dual doping from x = 0 to x = 0.1 which then declined until x = 0.3. The decrease in volume at higher doping content (x > 0.1) can be attributed to the higher compressive strain induced by the varying dopant sizes existing in the Bi_2Te_3 hexagonal structure. Tellurobismuthite semiconductors such as Bi_2Te_3 materials crystalizes into the hexagonal unit cell where the lattice parameter along the a-axis (4.374 Å) is much smaller than that of the c-axis (30.36 Å). The massive difference in the lattice parameters along difference directions brings about the crystal structure anisotropy. Therefore variable lattice distortion (contraction and expansion) coexisting in the Bi_2Te_3 structure upon doping is not uncommon[41]. This is because the lattice constants of the dopants overlap with that of the pristine material. In the case of the indium doped samples (In_2Te_3), the resulting composition consist of mixed lattice constant of Bi_2Te_3 and In_2Te_3 (a = b = c = 18.475 Å)[42]. These parameters overlap with that of Bi_2Te_3. Thus in less ($x \leq 0.1$) doped samples, minor distortion is observed, which slightly changes the lattice constant. However, for higher doping, the massive substitution of In^{3+} for Bi^{3+} decreases the lattice parameter, especially along the c-axis, thereby diminishing the lattice volume. Elsewhere, Samoilov et al. [41] have shown that single doping of indium in lead Telluride (PbTe) causes lattice parameter decrease for doping content (x) less than 0.6 at.%. However, as the In

concentration further increased (x > 0.6 at.%), a noticeable rise in the lattice parameter was observed. The estimated microstrain varied mildly for the less doped samples ($x \leq 0.1$) and largely for the highly doped (x > 0.1) compositions (**Figure S-6d**). The observed variation in the microstrain is attributed to the dual doping induced lattice imperfection.

We adopted the Scherer's relation [43] to estimate the average crystallite size **(Eqn 2)** and micro-strain **(Eqn 3)** of all the BIST (x = 0, 0.05,0.1, 0.2 ,0.3) samples.

$$\text{The average crystallite size } (S_{cryst}) = \frac{0.9\lambda}{\beta cos\theta} \quad (2)$$

and

$$\text{Microstrain } (\varepsilon) = \frac{\beta cos\theta}{4} \quad (3)$$

Where λ, β, and θ, are the wavelength of the X-ray used (1.5406Å), the full width at half maximum (FWHM, **Table S-3**) in radian along (015), and Bragg's diffraction angle respectively.

The calculated crystallite size and microstrain ranges from 80 nm, 4.3×10^{-4} for x = 0 to 32 nm, 10.943×10^{-4} for x = 0.3 respectively Similarly, the microstrain decreases with doping which is expected and concurrent with reported studies.[21,44]. The dual dopants – induced lattice dislocation (γ) is numerically calculated using **Eqn 4** [8] and the results is shown in **Table S-4**

$$(\gamma) = \frac{15\varepsilon}{aS_{cryst}} \quad (4)$$

where a is the lattice constant, ε is microstrain, and S_{cryst} is the average crystallite size.

It is evident from **Table S-4** that, the dislocation density increases in dual doping with the maximum γ found for BIST-0.3 **(** 11.8×10^{15})m^{-2}

Further, we have also used the Raman spectroscopy technique to characterize the BIST samples. The Raman peaks of the synthesized BIST (x = 0, 0.05, 0.1, 0.2 and 0.3) is shown in **Figure 3c** which elucidate the presence of two prominent peaks for A_{1u} (out of plane) and A_{1g} (in-plane) modes at 114.8 cm^{-1} and 137.4 cm^{-1} respectively. The A_{1u} peak shifts slightly for the less doped samples (x =

0.05 and 0.1). However, for the higher doping content (x = 0.2 and x = 0.3) all the Raman peaks were restored to that of Bi_2Te_3. **Figure 3d** shows the variation in the Raman shift with dual doping. Bi_2Te_3 comprises 15 normal modes at r point of the Brillion Zone [45,46] where r is related by **Eqn 5**

$$\Gamma = 2\left(A_{1g} + E_g\right) + 3(A_{2u} + E_u) \quad (5)$$

Where the "*g*" and "*u*" denote Raman active and infrared active (IR) modes, respectively. Richter et al. [47] observed the IR active mode in Bi_2Te_3 material at 94 cm^{-1} and 120 cm^{-1} corresponding to E_u and $A_{1u,}$ respectively, at RT.

Similarly, The XPS data obtained for the high-resolution spectra (Bi 4f; Te, Sb, In 3d) and full range survey scan are presented in **Figure 4** and **Figure S-7** respectively. The complete high-resolution spectra of the constituent components of BIST are fitted by typical Gaussian function, and the results are shown in **Figure 4** and **Table (S-5** and **S-6)**. The two prominent peaks each (156.847eV and 158.283 eV) and (162.169 and 163.632 eV) in **Figure 4a** for the pristine (x = 0) are assigned to Bi $4f_{7/2}$ and Bi $4f_{5/2}$ doublet respectively. It is observed that both the Bi $4f_{7/2}$ and Bi $4f_{5/2}$ shifted by ΔE = 0.3 – 0.6 (eV) with an increase in doping content. The shift in the binding energy to higher energy with doping is due to the substitutional effect of In in the Bi lattice.[48] For the XPS spectra of Te-3d are shown in **Figure 4b**. From the Te-3d data, two peaks situated at 576.96 eV and 586.88eV are well assigned to Te $3d_{5/2}$ and $3d_{3/2}$ [49,50] respectively. It is realized that upon the variation in the dopant amount, no significant change in the peak position is noticed for all the Te -3d spectra.

Figure 4c shows the XPS high-resolution spectra of Sb-3d.The binding energy for the Sb $3d_{5/2}$ and $3d_{3/2}$ for the least doped (x = 0.05) samples are 529.8eV and 539.4 eV respectively. This is similar to the reported values of Sb^{3+} chemical state. [49,51,52]. Upon increase in doping amount (x = 0.1, 0.2 and 0.3) the binding energies increase by approximately 0.1 eV and 0.05 eV for the Sb $3d_{5/2}$ and Sb $3d_{3/2}$ respectively. More so, the increase in XPS peak intensity for Sb $3d_{3/2}$ and In ($3d_{3/2}$ and $3d5_2$) signify even distribution of dopants in the host matrix.[53] Again **Figure 4d** shows the high-resolution spectra of In 3d core-level spectra. The binding energies at 445.14 eV and 452.48 eV is well assigned to In^{3+} $3d_{5/2}$ and $3d_{3/2}$ [50,54] respectively. As shown in **Figure 4d**, the splitting of In $3d_{5/2}$ peaks at a binding

energy of 440.7eV and 444.5eV indicates the existence of In(0) (440.7 eV) and In (III) (444.5 eV).[55] The presence of an additional peak at 440.76 eV is linked to different chemical bonding for In.

We performed the room-temperature Hall Effect measurement as well as the simultaneous measurement of the S and the σ of all our samples to show the dual doping impact on the pristine Bi_2Te_3 material. In **Table 1,** the Hall Effect results are compared with that from the ZEM measurement. A minimal variation between the σ_{Hall} and σ_{ZEM} was observed.

The measured electron density is in the range of $10^{19}cm^{-3,}$ which is typical for conventional thermoelectric materials.[2] The pristine material (x =0) responded to the introduction of the dopants, where a decrease in the electron mobility accompanies the electron density improvement as the doping content increases. It is worth mentioning that the structural complexity of the Bi_2Te_3 crystal domain increases upon the introduction of the dopants and hence offers opposition to conduction electrons. The impediment of the conduction electrons by the impurity atoms lead to a reduction in electron mobility.

The RT μ_H deterioration with doping content also indicates alloy scattering of carries.[56] Isovalent substitution of Bi^{3+} for In^{3+} is useful for creating neutral ions which control the excessive improvement in the electron density. This is useful because the large electron density compromises Seebeck coefficient (**Eqn 6**). From **Eqn 6**, we extracted the RT electron effective mass of all our samples using the single parabolic band Mott equation, and the result is shown in **Table 1**

$$S = \frac{8\pi^{8/3}K_B^2}{3^{5/3}\,eh^2}\,T\left(\frac{m^*}{n^{2/3}}\right) \qquad (6)$$

Where k_B is the Boltzmann constant ($1.3807 \times 10^{-23}\,JK^{-1}$), m^* is the effective mass, h is Planck's constant (6.626×10^{-34}J.s), and n is the electron density.

The experimentally estimated effective mass did not vary significantly with the dual doping (for $x \leq 0.1$) due to the slight difference in the electron density values. However for $x > 0.1$, the effective mass

varies significantly with an initial sharp increase for x = 0.2 which then drops slight for x = 0.3. This is expected for the large values of n_H for x = 0.2 (3.667×10^{19}cm^{-3}) and x = 0.3 (4.279×10^{19}cm^{-3}).

Figure 5 is the FEG-SEM morphology of all the synthesized dual doped samples, and the corresponding EDX is shown in **Figure S-2** and **Table S-7,** respectively. Nanocubes of varying sizes are observed for all the samples where the average crystallite size was estimated to increase from the pristine to BIST-0.05, which then decreases with further doping (**Figure S-6d**). The reduced crystallite size contributed to the enhanced thermal conductivity reduction. This is so because the smaller crystallite sizes increase the number of crystal boundaries, which eventually enhances grain boundary-induced phonon scattering and consequently reduced lattice thermal conductivity.

Considering the electronic configuration of In ($5s^2\ 5p^1$) occupying the Bi ($6s^2\ 6p^3$) site, lead to the formation of uncharged defects in In^*_{Bi} which is associated with the transition of $5s^2$ electrons of In to the 5p orbitals.[57], ie In ($5s^2\ 5p^1$) → In^*_{Bi} ($5s^0\ 5p^3$).[58] More so, when Bi atoms occupy Te site during the crystal synthesis and growth, a negatively charged anti-site defects are formed. The density of the anti-site defect, however, is dependent on the bond polarity.[59,60] The vast difference in the electronegativity value between In/Te compared to that of Bi/Te or Sb/Te lead to higher polarity of In-Te bonds. This thus increases the formation energy (E_{form}) of the anti-site defects for In/Te. As such, the substitution of Bi by In become more favourable due to the subdual of E_{form} of the anti-site defect instigated by the larger electronegativity difference between In-Te.

To investigate the contribution of dual doping on the band structure, we have estimated the experimental bandgap for all our samples. The peak Seebeck coefficient (S_{max}), and its corresponding temperature (T_{max}), is used with the aid of the Goldsmid – Sharp relation ($E_g = 2eT_{max}S_{max}$) to estimate the bandgap of all our samples and the result of which is shown in **Figure S-8a.** The experimentally determined band gap (**Figure S-8a**) decreases monotonically with doping from the pristine (E_g = 130 meV) to BIST- 0.2 (E_g = 118 meV) and then sharply to BIST- 0.3 (Eg = 94 meV). This is typical of most covalent semiconductors.[61] The decrease in bandgap with doping is detrimental to the Seebeck coefficient as the participation of minority charge carriers to conduction electrons emerges, which

improves n_H and hence decreases Seebeck coefficient [34]. Similarly, we have extracted the Fermi energy with respect to the conduction band ($E_F - E_C$) for all the BIST samples using **Eqn 7**. **Figure S-8b** shows the numerically determined $E_F - E_C$ for all our samples using the experimentally measured TE properties.[62]

$$\boldsymbol{S} = -\left(\frac{1}{3}\right)\frac{\pi^2 {K_B}^2}{e(E_F - E_C)}T \qquad (7)$$

Eqn 7 shows the inverse dependence of the Seebeck coefficient of the Fermi energy. At RT, the calculated E_F are 42.12, 48.38, 49.05, 49.6 and 62.01 meV for BT, BIST- 0.05, BIST- 0.1, BIST-0.2 and BIST- 0.3 respectively. As can be seen, the doping dependent Fermi energy gradually increases. Substitution of In^{3+} for Bi^{3+} induces neutral ions in the BIST structure, which is expected to inhibit escalation of the charge density as the doping content increases. The magnitude of the Seebeck coefficient increases slightly with temperature as the Fermi energy (**Figure S-8b**) approaches the minority carrier band. After the generation of minority carriers, the Seebeck coefficient drops with S_{max} of -175 μVK^{-1} (for x = 0)**.** The S_{max} shifted by 0.1, 0.14, 0.16 and 0.47 μVK^{-1} for BIST- 0.05, BIST- 0.1, BIST- 0.2 and BIST- 0.3 respectively. It is understood that the emergence of the Seebeck coefficient peak is linked to the onset of thermal excitation of both electrons and holes at high temperature [63]. However, the measured shift for the dual doped samples are far less than the uncertainty and can, therefore, be ignored. Again, at low temperatures, the population of minority carriers, although present but causes less deterioration to the Seebeck coefficient for BIST (ΔS=10 - 12 μVK^{-1}) compare to that of the pristine (ΔS=37 μVK^{-1}) probably due to presence of interband states.[64] More so, the obtained bandgap for the pristine (130meV) is comparable to literature values of 140 meV [65] but less than that reported elsewhere [1,17,66].

For the various BIST nanostructures studied, our DFT calculation reveals their band structure, as shown in **Figure 6**. These results elucidate the combined effect of the dual dopants on the band energy. The adopted mechanism of the dual isovalent doping does not merely transfer charges to the bands of the host Bi_2Te_3 semiconductor but also favours reordering of the core state present deep in the valence

band of the host. In this way, the impurity causes changes to the Fermi level, E_F, and hence increases the density of conducting charge carriers around the Fermi level. It is evident from **Figure 6(a – e)** that the introduction of the dual dopants (In and Sb) results in the decrease of the bandgap. The band diagrams (**Figure 6**) and the corresponding DOS diagrams (**Figure 7**) show that the computational results agree well with the experimentally determined values (**Figure S-8a** and **Table S-8**).

Similarly, the Fermi energy is lowered for less doping but increases for higher doping. More so, it is clear from the DOS diagrams (**Figure S-9**) that, as the dual dopant increases, the overall density of state near the Fermi level is improved coupled with a decrease in the conduction band minimum. This results in the enhancement of the electron density (**Table 1**) and hence deteriorates the Seebeck coefficient. The electronic structure calculation reveals the formation of deep defects states (-15 eV) in the valence band. The creation of deep states influences the electronic transport properties of the system. In this sense, increasing the impurity content creates a strong interaction between the deep states, which improves the DOS and hence the electron density. Similarly, there is a noticeable encroachment of the conduction band towards the Fermi energy. This idea of isovalent substitution is proven useful to the band structure by both the experimental and theoretical data for the bismuth telluride system.

Figure 8a is the temperature dependence of electrical conductivity (σ_{ZEM}) for all the BIST samples. The σ_{ZEM} of all the samples decreases with temperature as well as doping content from 300K to 473K. Although the electron concentration increases mildly with dual doping, the σ_{ZEM} decreases with both temperature and doping due to the sharp deterioration of the electron mobility ($\sigma_{ZEM} = ne\mu$). The vast decrease in mobility observed for the BIST samples signifies the enhanced electron-phonon scattering, which decreases the mean free path of conduction electrons[11].

The electrical conductivity dependence on temperature is fitted with $\sigma = aT^b$, whereby the magnitude of exponent gives clarity on the primary scattering mechanism [67]. The σ of all the samples exhibit a power-law dependence on temperature ($T^{-0.9}$ – $T^{-0.7}$) with increasing doping content. This is evident that the scattering mechanism is predominantly by acoustic phonon scattering due to the negative

values of b. Despite the absence of the ionized impurity scattering in all of the samples due to the isovalent doping, the Hall electron mobility deteriorates with doping which is principally due to the enhanced electron-phonon scattering [68] and lattice distortion induced scattering.[69] Similarly, the temperature-dependent electrical conductivity of the synthesized samples decreases with doping due to the presence of the larger residual resistivity, which is indicative of strong electron scattering caused by the dual dopants.[70] The manifestation of the decrease in the electrical conductivity with dual doping and temperature like in degenerate semiconductors suggest that the Fermi level E_F is in the vicinity of the conduction band.[71]

The measured Seebeck coefficient dependence on temperature is shown in **Figure 8b**. The RT Seebeck coefficient decreases with doping content. This is because of the increase in the electron density with increasing doping content. For the pristine Bi_2Te_3 sample, the Seebeck coefficient increases slightly from room 300K (-174 μVK^{-1}) until 360K and then declined afterwards to 473K with S_{max} = -175 μVK^{-1}. However, for the dual doped samples, the peak Seebeck coefficient shifts to a higher temperature (380K but lower S values) for all the BIST samples. The shift of S_{max} to a higher temperature for the dual doped BIST samples is because of the suppression of intrinsic excitation. [9][1] The temperature dependence of S for all the BIST ($0 \leq x \leq 0.3$) samples follow a similar trend with the Seebeck coefficient values ($S < 0$) demonstrating that all our samples show an n-type semiconductor behaviour throughout the entire temperature range. Again the Fermi energy of BIST-0.05, BIST- 0.1 and BIST- 0.2 at RT are similar, which is responsible for their comparable S values at 300K.

Figure 8c, is the calculated power factor obtained for all the synthesized BIST ($0 < x < 0.3$) samples. The PF dependence of both temperature (**Figure 8c**) and doping content (**Figure S-10**) at 300K are shown to degrade with doping. This is simply because of the simultaneous decrease in the electrical conductivity and Seebeck coefficient. The RT PF decreases exponentially from x = 0 (PF=10^{-3} $Wm^{-1}K^{-2}$) to x = 0.2 (PF= 0.5×10^{-3} $Wm^{-1}K^{-2}$) which then sharply decrease for x = 0.3 (PF = 0.16×10^{-3} $Wm^{-1}K^{-2}$). It is worth mentioning that at much higher doping content (x = 0.3), the mild increase in

the electron density is accompanied by a drastic decrease in electron mobility which simultaneously decreases S and σ. Bismuth telluride structures are already a complex structure with enough gaps to accommodate impurity atoms. Therefore, the dual doping of In and Sb enhances crystal lattice distortion[69] (**Figure 3b**), which thus hinder PF the dual doped samples. The sample with the best PF (10^{-3} $Wm^{-1}K^{-2}$) is seen in Bi_2Te_3 at 300K.

The transfer of heat by both electrons and quantized vibrations in all the BIST samples were investigated by measuring the thermal diffusivity (λ) (**Figure S-11a**) using the Laser Flash method. The heat capacity (C_p) and the density (ρ) is also obtained using the differential scanning calorimetry (DSC 404F) and Archimedes principle respectively. The total thermal conductivity (k_T) is readily calculated from the relation, $\kappa_T = \lambda \times \rho \times C_p$ and the result of which is shown in **Figure 8d**

Therefore, it was necessary to estimate the electronic (k_{el}) as well as lattice (k_{lat}) contribution to the total thermal conductivity. Here, k_{el} is calculated using the Wiedeman Franz law; $\kappa_{el} = L\sigma T$, where, L is the Lorentz number, which is estimated, using **Eqn (S-2),** σ is the measured electrical conductivity and T is the temperature in (K). The obtained data for the calculated L and k_{el} is displayed in **Figure S-11 (b and c),** respectively. So, by using $\kappa_T = k_{el} + k_{lat}$, the corresponding k_{lat} values are derived, which is shown in **Figure S-11d.** The lattice thermal conductivity significantly decreases as the doping content increases due to synergy of enhanced phonon scattering instigated by small crystallite size, lattice distortion, microstrain of the In and Sb impurities atoms. It is to be noted that if thermal excitation of minority carrier is dominant, an upturn of the thermal conductivity would have been seen at high temperature [72]. Thus, the observed lattice distortion, small crystallite size and enhanced microstrain in all the dual doped samples is responsible for the low thermal conductivity (K_T) in all the dual doped samples compared to the pristine. The small crystallite size enhances grain boundaries scattering, which thus offers opposition to phonon transport and hence reduces the total thermal conductivity. More so, excessive doping in Bi_2Te_3 thermoelectric materials can cause increase in thermal conductivity due to agglomeration of the excess dopants [73]. In our dual doped samples, for $x \leq 0.1$ yielded an enhanced crystalline quality with improved thermal properties. As the doping

content is further increased (x > 0.1), agglomeration occurs (**Figure 5 c and d**). The degradation of the crystallinity (leading to a multifold decrease in mobility and electrical conductivity) and agglomeration of the excess dopants in the host matrix, causes a rise in the thermal conductivity for the highly doped samples (x ≥ 0.2). Similar behaviour is reported by *Cao et al*. [73] for CNT doped Bi_2Te_3, where the CNT content initially promoted a decrease in thermal conductivity. However, when the doping amount surpasses 0.5%, the thermal conductivity tends to increase [73]. Elsewhere Khasimsaheb *et al*. [74] demonstrated that CNT dispersion up to 0.025% effectively reduces the total thermal conductivity through phonon scattering by the interfaces and boundaries of the CNT/PbTe matrix. For excess doping (higher than 0.025%), K_T increases afterwards. This trend of the thermal conductivity behaviour is attributed to the agglomeration of the excess dopants in the host matrix.

It is, therefore, crucial to mention that, although the presence of an impurity in a host matrix is beneficial for enhancing phonon scattering, excessive doping can weaken the dispersion of lattice vibration [75] and therefore affect the thermal conductivity. For this reason, an optimum impurity content is required to achieve a synergistic effect of the thermoelectric performance. The minimum thermal conductivity in this work (K_T = 0.35 $Wm^{-1}K^{-1}$ for BIST- 0.2) is lower than that of Yang *et al*. [18] (0.58$Wm^{-1}K^{-1}$), Wang *et al*.[76] (0.5 $Wm^{-1}K^{-1}$), Li *et al*.[77] (> 0.6 $Wm^{-1}K^{-1}$). The ultralow thermal conductivity obtained in this work is compared to most recent studies (**Table S-9**) regarding doped Bi_2Te_3 thermoelectric materials.

In **Figure 8e**, we have shown the calculated ZT dependence on temperature using the measured electrical conductivity, Seebeck coefficient (**Figure 8b**) and the total thermal conductivity (**Figure 8d**). The maximum figure of merit (ZT = 0.57) is found for BIST- 0.1 at 423K (**Figure 8f**) which is 47% more than the pristine (ZT = 0.388). The higher ZT obtained for BIST-0.1 is due to the adequate compensation of the smaller power factor by the ultralow K_T. Thus dual isovalent inclusion strategy offers excellent potential for further enhancing the TE performance in Bi_2Te_3 TE materials.

4. Conclusion

Dual doping of Sb and In in Bi_2Te_3 TE material has been successfully synthesized through a method modified from that of Wang *et al.*. After the optimization study of the Bi_2Te_3 material via post-synthesis treatment, the best sample was further enhanced via dual doping with In and Sb. Similarly, the electronic and heat transport properties were studied to elucidate the TE performance of the dual doped compositions. Our DFT calculation reveals the band structures and PDOS, which clarify the combined effect of the dual dopants on the band energy and the density of state effective mass near the Fermi level. The presence of the deep defect states in the valence band influences the electronic transport properties of the system, which thus contribute to the enhancement in the TE performance via DOS optimization. It is shown that the dual doping of In and Sb significantly degrade the Hall electron mobility with a mild improvement in n_H. The degradation of mobility is attributed to the structure complexity induced lattice distortion, which affects the transport of conduction electrons and hence improve the electron and phonon scattering. This is seen in the ultralow lattice thermal conductivity, total thermal conductivity and thus enhances the TE performance of the BIST samples. A maximum ZT of 0.57 at 423K is achieved for BIST-0.1. It is therefore apparent that the ultra-low thermal conductivity observed in the BIST- 0.1 sample compensated for the decrease in both electrical conductivity and Seebeck coefficient and thus improves the TE performance of all the dual doped samples.

Acknowledgement

We wish to acknowledge grants from the Research Grants Council of Hong Kong Special Administrative Region Project no. T42-103/16N. VK acknowledges Act 211 Government of the Russian Federation, contract No. 02.A03.21.0011

References

[1] L. Yang, Z. G. Chen, M. S. Dargusch, J. Zou, *Adv. Energy Mater.* **2018**, *8*, 1.

[2] G. J. Snyder, E. S. Toberer, *Nat. Mater.* **2008**, *7*, 105.

[3] C. Han, Q. Sun, Z. Li, S. X. Dou, *Adv. Energy Mater.* **2016**, DOI 10.1002/aenm.201600498.

[4] E. Kioupakis, M. L. Tiago, S. G. Louie, *Phys. Rev. B - Condens. Matter Mater. Phys.* **2010**, *82*, 1.

[5] Z. M. Gibbs, H. S. Kim, H. Wang, G. J. Snyder, *Appl. Phys. Lett.* **2015**, *106*, DOI 10.1063/1.4905922.

[6] D. Palit, S. K. Srivastava, M. C. Chakravorti, B. K. Samantaray, *Mater. Chem. Phys.* **1997**, *49*, 22.

[7] T. K. Mandal, S. K. Srivastava, B. K. Samantaray, B. K. Mathur, *Mater. Sci. Eng. B Solid-State Mater. Adv. Technol.* **1999**, *64*, 143.

[8] P. Desai, D. D. Patel, A. R. Jani, *J. Cryst. Growth* **2014**, *390*, 12.

[9] T. Zhang, X. Su, Y. Yan, W. Liu, T. Hu, C. Zhang, Z. Zhang, X. Tang, *ACS Appl. Mater. Interfaces* **2018**, *10*, 22389.

[10] B. C. Sales, D. Mandrus, R. K. Williams, *Science.* **1996**, *272*, 1325.

[11] H. Cho, J. H. Kim, S. Y. Back, K. Ahn, J. S. Rhyee, S. D. Park, *J. Alloys Compd.* **2018**, *731*, 531.

[12] A. A. Usenko, D. O. Moskovskikh, M. V. Gorshenkov, A. V. Korotitskiy, S. D. Kaloshkin, A. I. Voronin, V. V. Khovaylo, *Scr. Mater.* **2015**, *96*, 9.

[13] M. S. Dresselhaus, G. Chen, M. Y. Tang, R. Yang, H. Lee, D. Wang, Z. Ren, J. P. Fleurial, P. Gogna, *Adv. Mater.* **2007**, *19*, 1043.

[14] R. Chen, R. Diaz, A. I. Hochbaum, R. Chen, R. D. Delgado, W. Liang, E. C. Garnett, M.

Najarian, *Nature* **2008**, *451*, 163.

[15] S. K. Bux, R. G. Blair, P. K. Gogna, H. Lee, G. Chen, M. S. Dresselhaus, R. B. Kaner, J. P. Fleurial, *Adv. Funct. Mater.* **2009**, *19*, 2445.

[16] J. R. Szczech, J. M. Higgins, S. Jin, *J. Mater. Chem.* **2011**, *21*, 4037.

[17] M. Hong, T. C. Chasapis, Z. G. Chen, L. Yang, M. G. Kanatzidis, G. J. Snyder, J. Zou, *ACS Nano* **2016**, *10*, 4719.

[18] L. Yang, Z. G. Chen, M. Hong, G. Han, J. Zou, *ACS Appl. Mater. Interfaces* **2015**, *7*, 23694.

[19] J.-D. Musah, X. Yanjun, A. M. Ilyas, T. G. Novak, S. Jeon, C. Arava, S. V. Novikov, D. S. Nikulin, W. Xu, L. Liu, A. Md, K.-H. Lam, X. Chen, C.-M. Lawrence Wu, V. A. L. Roy, *ACS Appl. Mater. & Interfaces* **2019**, *11*, 44026.

[20] L. Wu, X. Li, S. Wang, T. Zhang, J. Yang, W. Zhang, L. Chen, **2017**, 1.

[21] A. J. Khimani, S. H. Chaki, M. P. Deshpande, J. P. Tailor, *J. Cryst. Growth* **2019**, *507*, 180.

[22] I. J. Ohsugi, D. Tokunaga, M. Kato, S. Yoneda, Y. Isoda, *Mater. Res. Innov.* **2015**, *19*, S5301.

[23] C. Guo, S. Wei, S. Zhou, T. Zhang, Z. Wang, S. Ng, X. Lu, C. L. Wu, W. Guo, **2017**, *2*, DOI 10.1021/acsami.7b07945.

[24] M. Nolan, S. Grigoleit, D. C. Sayle, S. C. Parker, G. W. Watson, **2005**, *576*, 217.

[25] J. Zhang, C. Liu, X. Zhang, F. Ke, Y. Han, G. Peng, Y. Ma, C. Gao, *Appl. Phys. Lett.* **2013**, *103*, DOI 10.1063/1.4816758.

[26] P. Bindu, S. Thomas, *J. Theor. Appl. Phys.* **2014**, *8*, 123.

[27] J. M. Schultz, J. P. McHugh, W. A. Tiller, *J. Appl. Phys.* **1962**, *33*, 2443.

[28] K. M. F. Shahil, M. Z. Hossain, D. Teweldebrhan, A. A. Balandin, *Appl. Phys. Lett.* **2010**, *96*, 1.

[29] D. Li, X. Y. Qin, Y. F. Liu, N. N. Wang, C. J. Song, R. R. Sun, *RSC Adv.* **2013**, *3*, 2632.

[30] M. S. Iovu, E. I. Kamitsos, C. P. E. Varsamis, P. Boolchand, M. Popescu, *Chalcogenide Lett.* **2005**, *2*, 21.

[31] K. Singkaselit, A. Sakulkalavek, R. Sakdanuphab, *Adv. Nat. Sci. Nanosci. Nanotechnol.* **2017**, *8*, DOI 10.1088/2043-6254/aa7222.

[32] L. Hu, T. Zhu, X. Liu, X. Zhao, *Adv. Funct. Mater.* **2014**, *24*, 5211.

[33] Y. Pan, T. R. Wei, C. F. Wu, J. F. Li, *J. Mater. Chem. C* **2015**, *3*, 10583.

[34] E. D. M. Rowe, D. Ph, D. Sc, F. Group, *Thermoelectrics Handbook: Macro to Nano*, **2006**.

[35] L. P. Hu, X. H. Liu, H. H. Xie, J. J. Shen, T. J. Zhu, X. B. Zhao, *Acta Mater.* **2012**, *60*, 4431.

[36] Y. Zhao, J. S. Dyck, B. M. Hernandez, C. Burda, *J. Phys. Chem. C* **2010**, *114*, 11607.

[37] Y. Liu, Q. Wang, J. Pan, Y. Sun, L. Zhang, S. Song, *Chem. - A Eur. J.* **2018**, *24*, 9765.

[38] Z. Wei, T. Xia, J. Ma, W. Feng, J. Dai, Q. Wang, P. Yan, *Mater. Charact.* **2007**, *58*, 1019.

[39] D. Liu, J. Sto, M. Seyring, M. Dru, X. Li, R. Schmechel, M. Rettenmayr, *Cryst. Growth Des.* **2016**, *16*, 617.

[40] R. Cao, H. Song, W. Gao, E. Li, X. Li, X. Hu, **2017**, *727*, 326.

[41] A. M. Samoilov,A.M. ; Buchnev, S. A. ; Dolgopolova, E. A. ; Yu.V. Synorov; Khoviv, *Inorg. Mater.* **2004**, *40*, 349.

[42] S. Yamanaka, M. Ishimaru, A. Charoenphakdee, H. Matsumoto, K. Kurosaki, **2009**, *38*, 1392.

[43] R. K. Rajakarthikeyan, S. Muthukumaran, *Opt. Mater. (Amst).* **2017**, *69*, 382.

[44] G. W. Y Ge, Y Guo, W Shi, Y Qiu, *J. shanghai Univ.* **2007**, *11(4)*, 403.

[45] V. Wagner, **1978**, *311*, 311.

[46] S. M. Souza, D. M. Trichês, C. M. Poffo, J. C. De Lima, T. A. Grandi, R. S. De Biasi, *J. Appl. Phys.* **2011**, *109*, DOI 10.1063/1.3520658.

[47] W. Richter, H. Kohler, C. R. Becker, *Phys. Stat. Sol.* **1977**, *84*, 619.

[48] B. Chen, J. Li, M. Wu, L. Hu, F. Liu, W. Ao, Y. Li, H. Xie, C. Zhang, *ACS Appl. Mater. Interfaces* **2019**, *11*, 45746.

[49] S. S. Garje, D. J. Eisler, J. S. Ritch, M. Afzaal, P. O'Brien, T. Chivers, *J. Am. Chem. Soc.* **2006**, *128*, 3120.

[50] S. Zhang, J. Zhang, B. Liu, X. Jia, G. Wang, H. Chang, *Sci. Rep.* **2019**, *9*, 1.

[51] L. Tan, A. Tang, Y. Zou, M. Long, Y. Zhang, J. Ouyang, J. Chen, *Sci. Rep.* **2017**, *7*, 1.

[52] R. Jin, G. Chen, J. Pei, J. Sun, Y. Wang, *Nanoscale* **2011**, *3*, 3893.

[53] M. V. Elizarov, O. V. Lozkina, D. I. Yeletz, A. V. Emeline, V. K. Ryabchuk, A. A. Murashkina, *J. Phys. Conf. Ser.* **2018**, *993*, DOI 10.1088/1742-6596/993/1/012004.

[54] G. G. Khan, S. Ghosh, A. Sarkar, G. Mandal, G. D. Mukherjee, U. Manju, N. Banu, B. N. Dev, *J. Appl. Phys.* **2015**, *118*, DOI 10.1063/1.4928952.

[55] D. P. Durkin, T. Ye, J. Choi, K. J. T. Livi, H. C. D. Long, P. C. Trulove, D. H. Fairbrother, L. M. Haverhals, D. Shuai, *Appl. Catal. B Environ.* **2018**, *221*, 290.

[56] L. P. Hu, T. J. Zhu, Y. G. Wang, H. H. Xie, Z. J. Xu, X. B. Zhao, *NPG Asia Mater.* **2014**, *6*, 1.

[57] L. Horak, J., Lostak, P., & Benes, *Philos. Mag.* **1984**, *50(6)*, 665.

[58] L. P. Hu, T. J. Zhu, X. Q. Yue, X. H. Liu, Y. G. Wang, Z. J. Xu, X. B. Zhao, *Acta Mater.* **2015**, *85*, 270.

[59] J. Horák, K. Čermák, L. Koudelka, *J. Phys. Chem. Solids* **1986**, *47*, 805.

[60] Z. Starý, J. Horák, M. Stordeur, M. Stölzer, *J. Phys. Chem. Solids* **1988**, *49*, 29.

[61] W. G. Zeier, A. Zevalkink, Z. M. Gibbs, G. Hautier, M. G. Kanatzidis, G. J. Snyder, *Angew. Chemie - Int. Ed.* **2016**, *55*, 6826.

[62] Y. H. Zhu, W. Bin Su, J. Liu, Y. C. Zhou, J. Li, X. Zhang, Y. Du, C. L. Wang, *Ceram. Int.* **2015**, *41*, 1535.

[63] M. Hong, Z. G. Chen, J. Zou, *Chinese Phys. B* **2018**, *27*, DOI 10.1088/1674-1056/27/4/048403.

[64] D. K. C. MacDonald, *Thermoelectricity: An Introduction to the Principles*, Dover Publications, INC, **2006**.

[65] I. T. Witting, T. C. Chasapis, F. Ricci, M. Peters, N. A. Heinz, G. Hautier, G. J. Snyder, *Adv. Electron. Mater.* **2019**, *5*, 1.

[66] M. S. Park, J. H. Song, J. E. Medvedeva, M. Kim, I. G. Kim, A. J. Freeman, *Phys. Rev. B - Condens. Matter Mater. Phys.* **2010**, *81*, 2.

[67] J. Navrátil, J. Horák, T. Plecháček, S. Kamba, P. Lošťák, J. S. Dyck, W. Chen, C. Uher, *J. Solid State Chem.* **2004**, *177*, 1704.

[68] S. Wang, G. Tan, W. Xie, G. Zheng, H. Li, J. Yang, X. Tang, *J. Mater. Chem.* **2012**, *22*, 20943.

[69] T. Zhu, Z. Xu, J. He, J. Shen, S. Zhu, L. Hu, T. M. Tritt, X. Zhao, *J. Mater. Chem. A* **2013**, *1*, 11589.

[70] Y. S. Hor, P. Roushan, H. Beidenkopf, J. Seo, D. Qu, J. G. Checkelsky, L. A. Wray, D. Hsieh, Y. Xia, S. Y. Xu, D. Qian, M. Z. Hasan, N. P. Ong, A. Yazdani, R. J. Cava, *Phys. Rev. B - Condens. Matter Mater. Phys.* **2010**, *81*, DOI 10.1103/PhysRevB.81.195203.

[71] R. Devender; Pascal, Gehring; Andrew, Gaul; Alexander, Hoyer; Kristina, Vaklinova; Rutvik, J. Mehta; Marko, Burghard; Theodorian, Borca - Tasciuc; David, J.Singh; Klaus, Kern; Ganpati, *Adv. Mater.* **2016**, 6436.

[72] K. Biswas, J. He, I. D. Blum, C. I. Wu, T. P. Hogan, D. N. Seidman, V. P. Dravid, M. G. Kanatzidis, *Nature* **2012**, *489*, 414.

[73] R. Cao, Z. Zhu, X. Jian, L. Xing, H. Hongzhang, *Appl. Phys. A* **2019**, *0*, 0.

[74] B. Khasimsaheb, N. Kumar, S. Bathula, B. Gahtori, D. Haranath, S. Neeleshwar, *Curr. Appl. Phys.* **2017**, *17*, 306.

[75] D. Li, X. Y. Qin, Y. J. Gu, *Mater. Res. Bull.* **2006**, *41*, 282.

[76] Y. Wang, W. Di Liu, H. Gao, L. J. Wang, M. Li, X. L. Shi, M. Hong, H. Wang, J. Zou, Z. G. Chen, *ACS Appl. Mater. Interfaces* **2019**, *11*, 31237.

[77] J. Li, Y. Xie, C. Zhang, K. Ma, F. Liu, W. Ao, Y. Li, C. Zhang, *ACS Appl. Mater. Interfaces* **2019**, *11*, 20064.

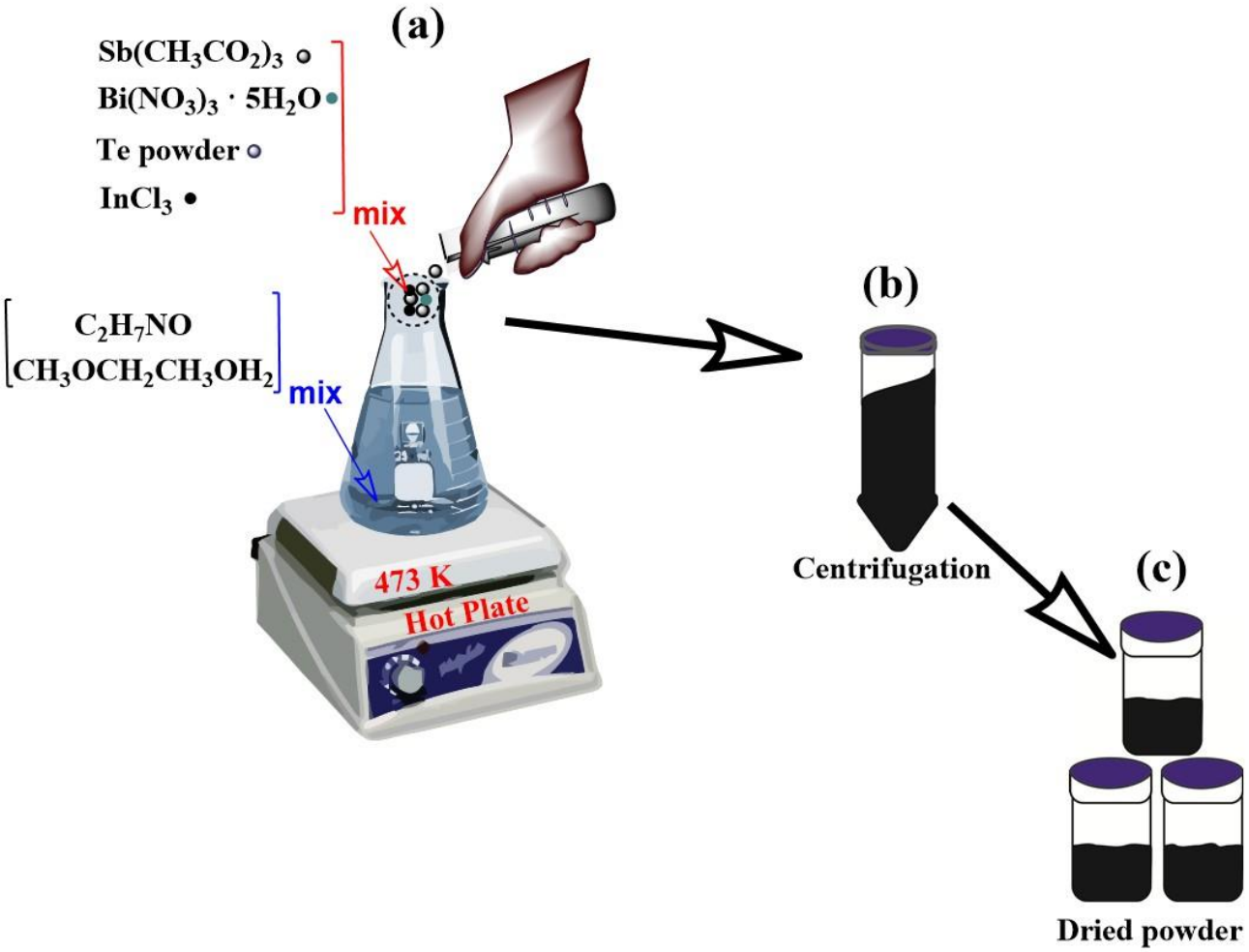

Figure 1. Schematic detail of the synthesis procedure (a) the precursors are mixed with ethanolamine – C_2H_7NO and 2-methoxyethanol - $CH_3OCH_2CH_3OH_2$ and then heated for 3 hours on hot plate , 473 K (b) the precipitate is collected, centrifuged and then dried (c) the obtained dried $Bi_{2-x}In_xSb_{2x/3}Te_3$ (x = 0, 0.05, 0.1, 0.2, 0.3) powder

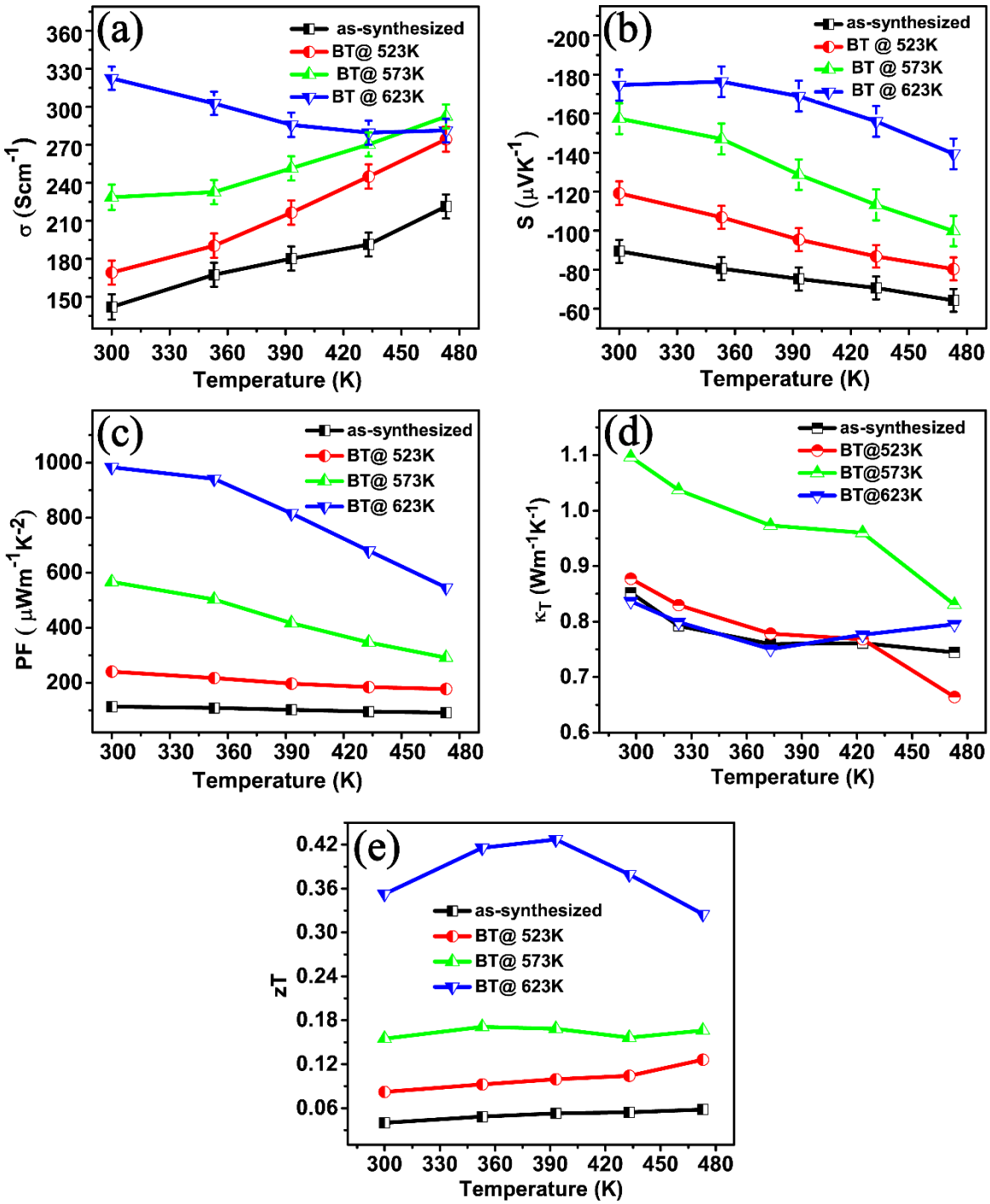

Figure 2. Temperature dependence of thermoelectric properties (a) measured electrical conductivity (b) measured Seebeck coefficient (c) calculated power factor (d) calculated total thermal conductivity and (c) calculated ZT of the as-synthesized, BT@523K, BT@573K and BT@623K samples.

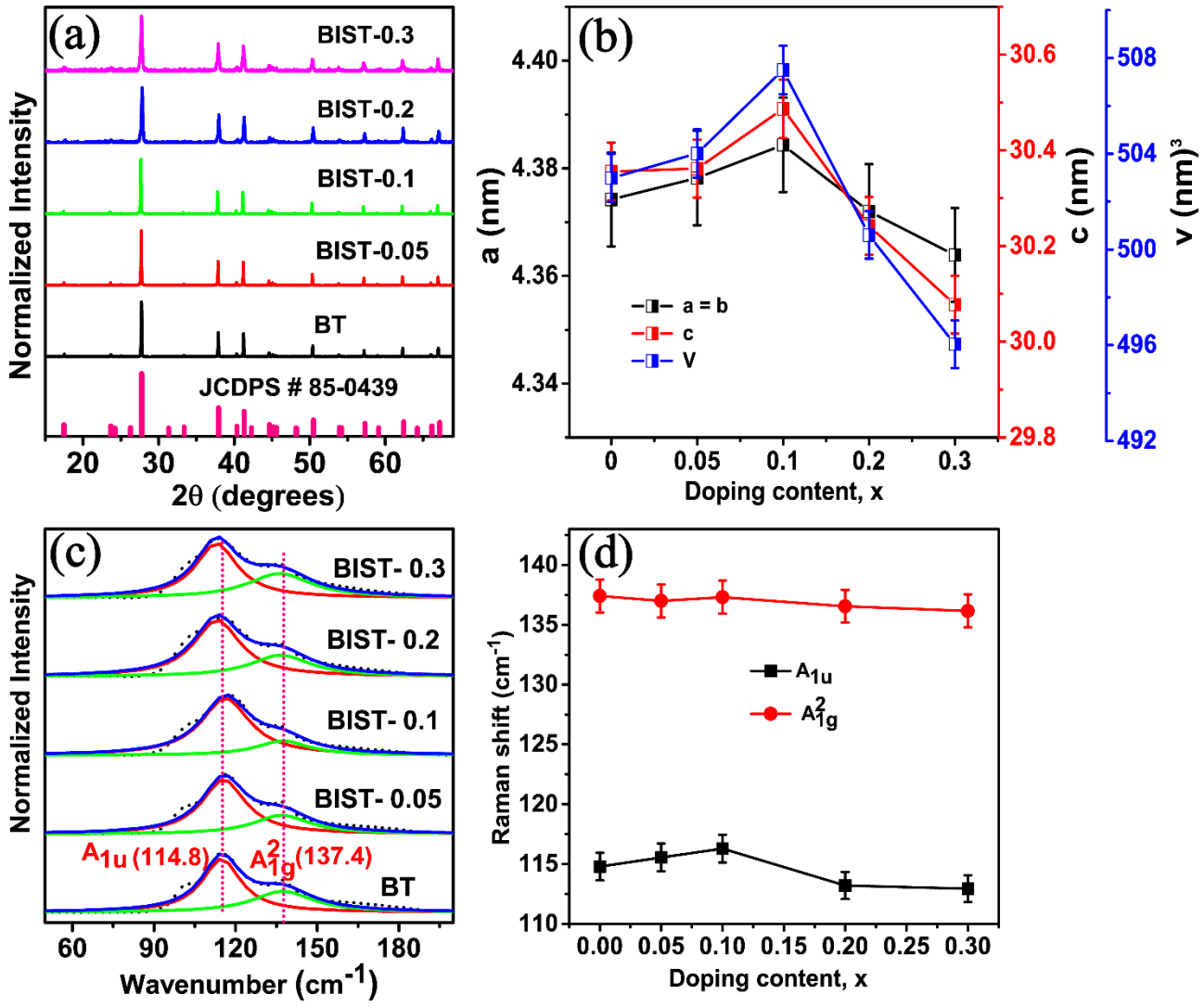

Figure 3. (a) the normalized XRD patterns ((b) calculated lattice parameters and volume (c) the Raman spectra (d) the Raman shift of all the synthesized BIST samples

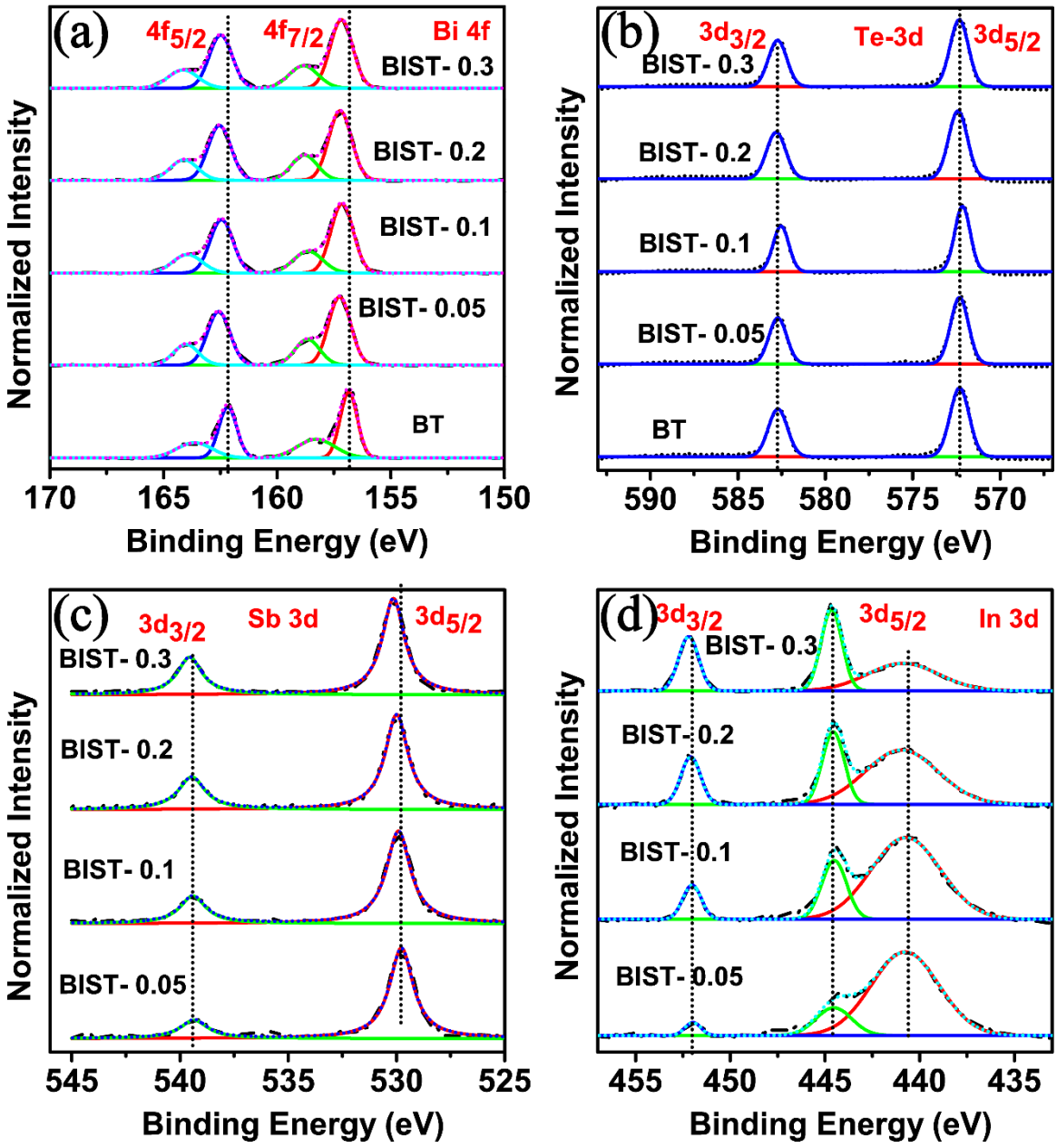

Figure 4. XPS. High resolution spectra of (a) Bi 4f (b) Te 3d (c) Sb 3d and (d) In 3d core-level for all the BIST samples

Table 1. Room temperature TE properties of BIST materials and the experimentally calculated m*

Samples	n_{Hall} $(10^{19} cm^{-3})$	μ_{Hall} $(cm^2 V^{-1} s^{-1})$	σ_{Hall} (Scm^{-1})	σ_{ZEM} (Scm^{-1})	S $(\mu V K^{-1})$	κ_T $(Wm^{-1}K^{-1})$	m* (m_e)
BT	1.71	137.22	325.57	328.87	-174.62	0.84	0.57
BIST-0.05	1.94	81.35	252.12	299.93	-151.52	0.57	0.54

BIST-0.1	2.07	61.68	204.89	246.12	-149.43	0.39	0.56
BIST-0.2	3.67	39.09	229.54	218.42	-147.79	0.26	0.81
BIST-0.3	4.28	13.25	90.81	118.51	-118.23	0.80	0.72

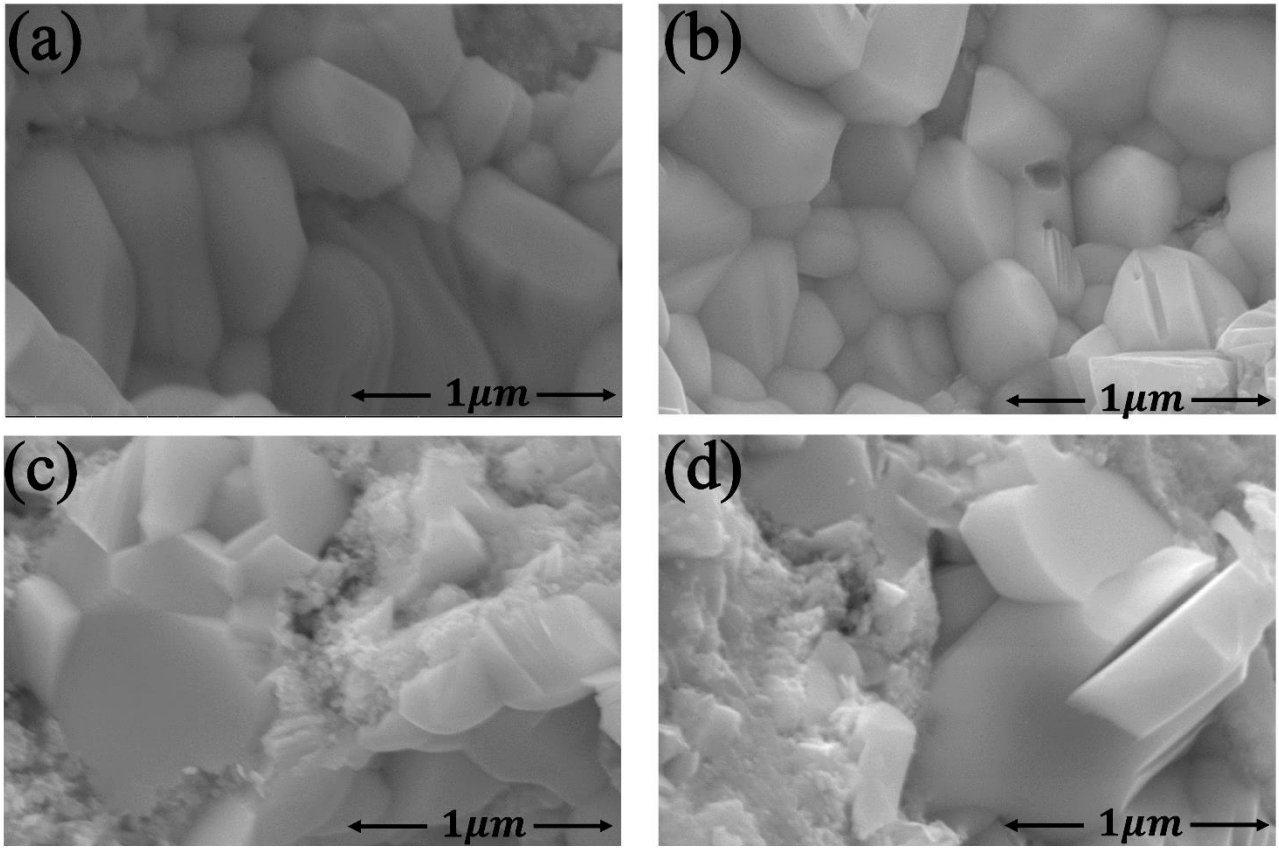

Figure 5 FEG-SEM of all the dual doped samples (a) BIST-0.05 (b) BIST-0.1 (c) BIST-0.2 (d) BIST-0.3

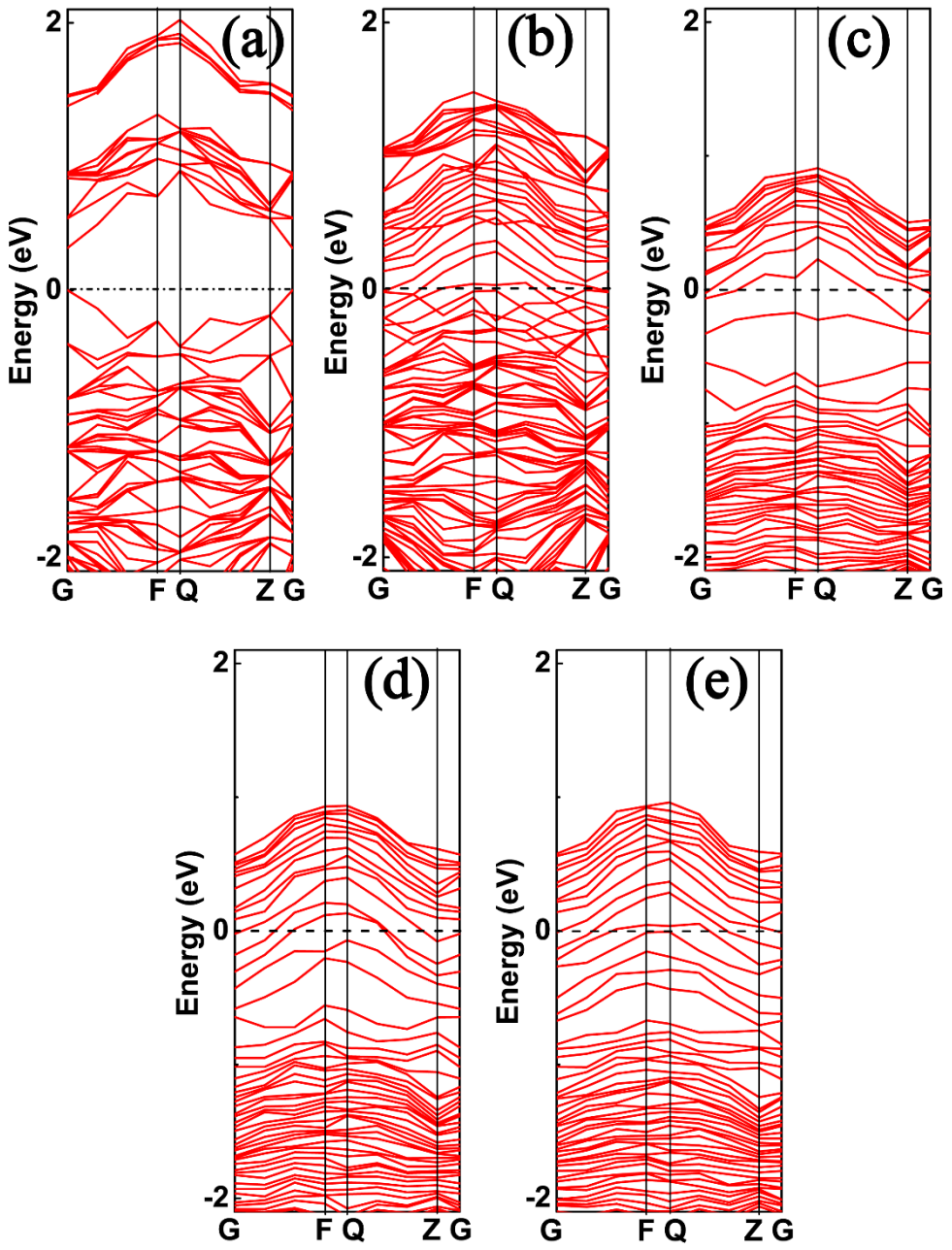

Figure 6 The calculated band structure for (a) pristine Bi_2Te_3 (b) BIST-0.05 (c) BIST-0.1 (d) BIST-0.2 (e) BIST-0.3

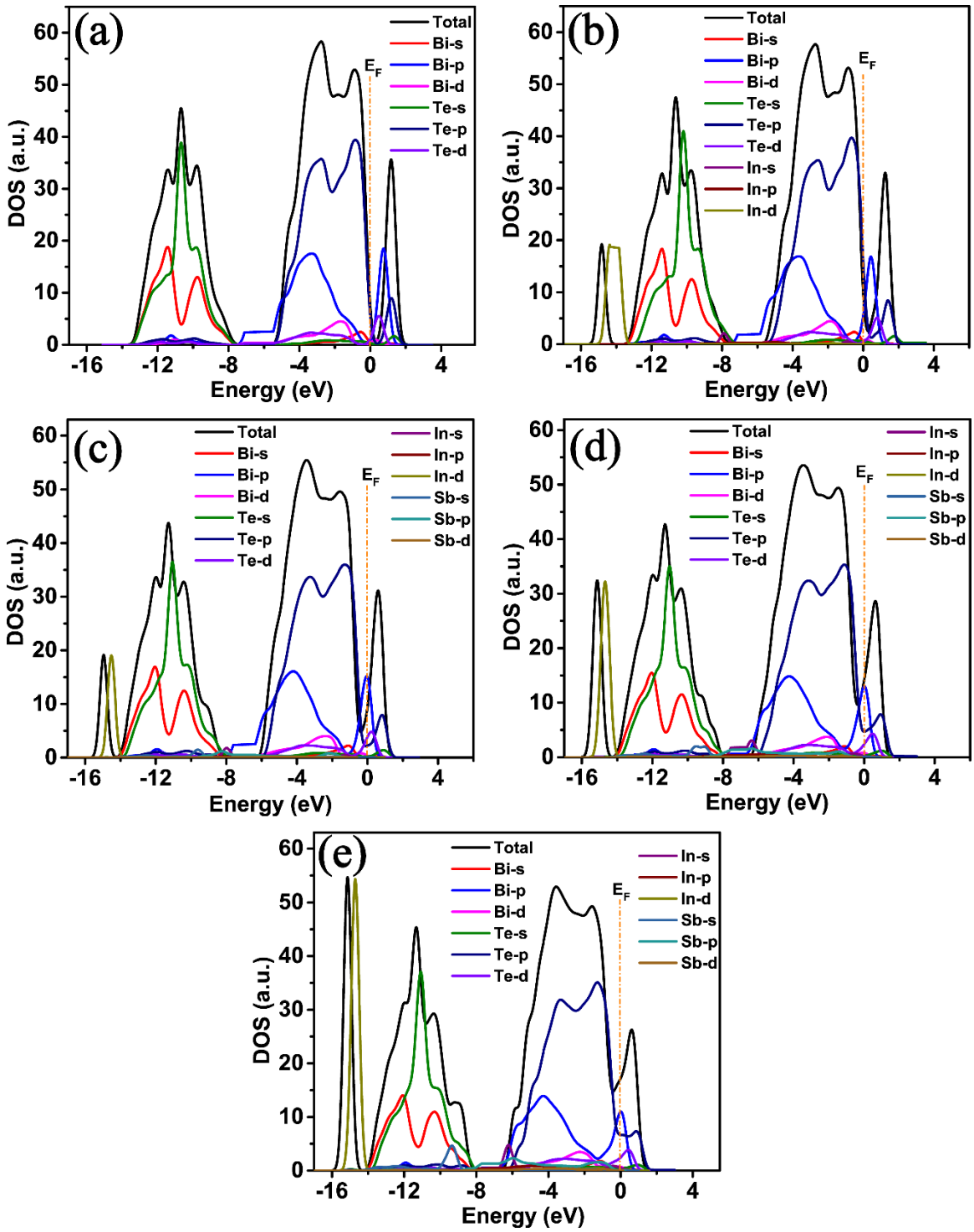

Figure 7 The calculated projected density of state (PDOS) of (a) pristine Bi_2Te_3 (b) BIST-0.05 (c) BIST-0.1 (d) BIST-0.2 (e) BIST-0.3

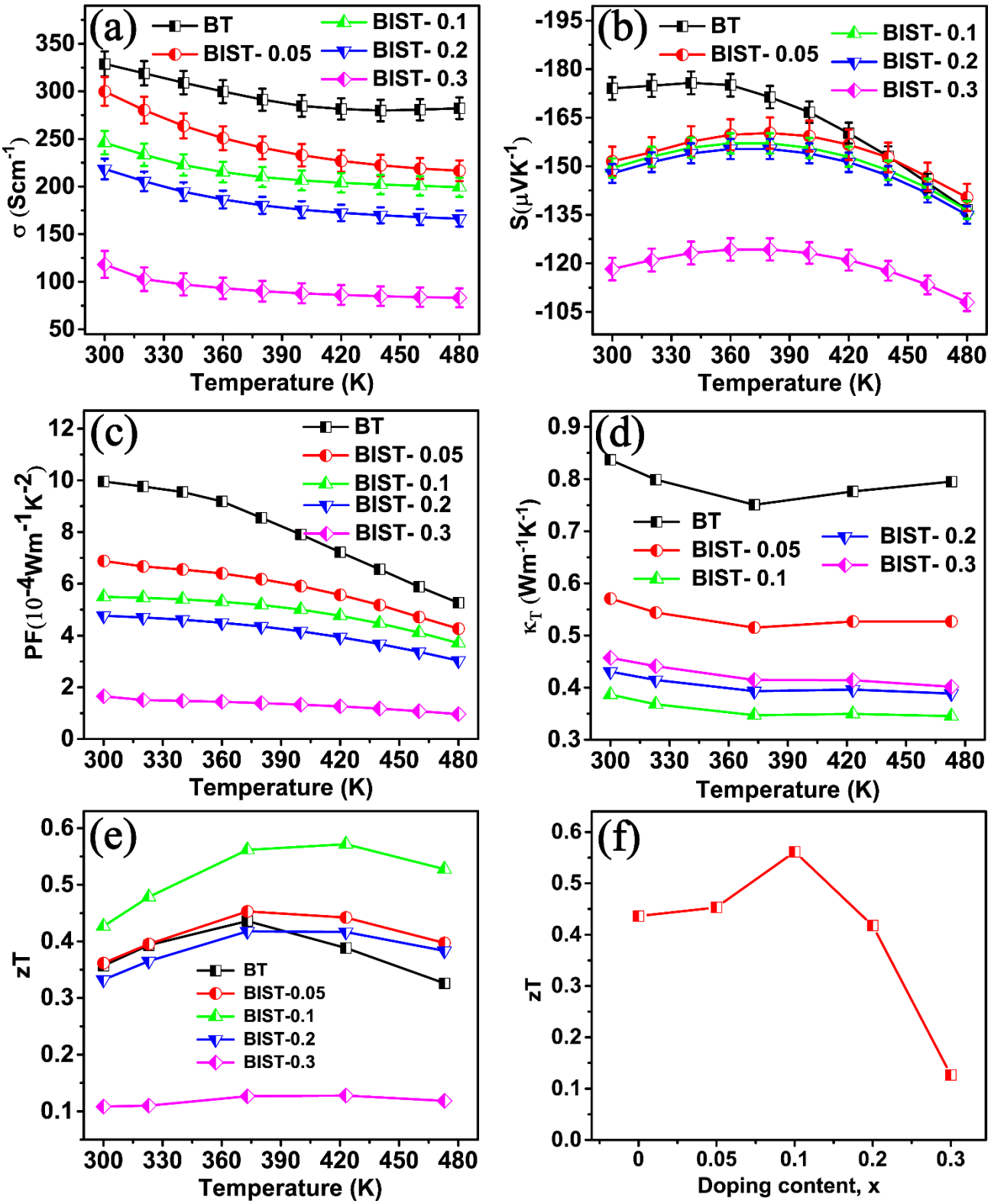

Figure 8. Temperature dependence of the (a) electrical conductivity (b) Seebeck coefficient (a) calculated power factor (d) the total thermal conductivity (e) the thermoelectric figure of merit (ZT) dependence on Temperature (f) the maximum ZT dependence on doping content at 423K for all the BIST samples